# Leaky-wave metasurfaces for integrated photonics

Heqing Huang<sup>1,†</sup>, Adam C. Overvig<sup>1,2,†</sup>, Yuan Xu<sup>1</sup>, Stephanie C. Malek<sup>1</sup>, Cheng-Chia Tsai<sup>1</sup>,

Andrea Alù<sup>2,3,\*</sup>, and Nanfang Yu<sup>1,\*</sup>

<sup>1</sup>Department of Applied Physics and Applied Mathematics, Columbia University, New York, NY 10027, USA.

<sup>2</sup>Photonics Initiative, Advanced Science Research Center, City University of New York, New York, NY 10031, USA

 $^3$ Physics Program, Graduate Center of the City University of New York, New York, NY 10016, USA  $^\dagger$ Authors contributed equally

\*Corresponding authors: <a href="mailto:ny2214@columbia.edu">ny2214@columbia.edu</a>, <a href="mailto:aalu@gc.cuny.edu">aalu@gc.cuny.edu</a>

## **Abstract**

Metasurfaces have been rapidly advancing our command over the many degrees of freedom of light within compact, lightweight devices. However, so far, they have mostly been limited to manipulating light in free space. Grating couplers provide the opportunity of bridging far-field optical radiation and in-plane guided waves, and thus have become fundamental building blocks in photonic integrated circuits. However, their operation and degree of light control is much more limited than metasurfaces. Metasurfaces integrated on top of guided wave photonic systems have been explored to control the scattering of light off-chip with enhanced functionalities – namely, point-by-point manipulation of amplitude, phase or polarization. However, these efforts have so far been limited to controlling one or two optical degrees of freedom at best, and to device configurations much more complex compared to conventional grating couplers. Here, we introduce leaky-wave metasurfaces, which are based on symmetrybroken photonic crystal slabs that support quasi-bound states in the continuum. This platform has a compact form factor equivalent to the one of conventional grating couplers, but it provides full command over amplitude, phase and polarization (four optical degrees of freedom) across large apertures. We present experimental demonstrations of various

functionalities for operation at  $\lambda=1.55~\mu m$  based on leaky-wave metasurfaces, including devices for phase and amplitude control at a fixed polarization state, and devices controlling all four optical degrees of freedom. Our results merge the fields of guided and free-space optics under the umbrella of metasurfaces, exploiting the hybrid nature of quasi-bound states in the continuum, for opportunities to advance in disruptive ways imaging, communications, augmented reality, quantum optics, LIDAR, and integrated photonic systems.

### Introduction

A monochromatic optical wavefront in free-space is characterized by four degrees of freedom at each point in space,  $(A, \Phi, \psi, \chi)$ : its amplitude A, phase  $\Phi$ , and polarization state, with elliptical parameters  $\psi$  and  $\chi$  representing polarization orientation and ellipticity, respectively. Manipulation of these degrees of freedom is among the key goals of contemporary photonics research. Metasurfaces [1]-[3] – flat optical devices composed of arrays of subwavelength scatterers – have been offering a flexible and powerful platform for producing desired wavefronts starting from unpatterned plane waves incident from free space, effectively compactifying table-top optical setups into multifunctional thin films [4]. Metasurfaces at optical frequencies have been widely used to spatially manipulate phase, but have also been shown to manipulate amplitude and phase [5],[6], phase and polarization state [7],[8], and recently all four parameters simultaneously [9]-[12] and beyond [13]. These concepts can be leveraged to an even larger extent in the radio-frequency (RF) spectrum, for which multi-layered fabrication and the large conductivity of metals enable exquisite and deeply subwavelength control of electromagnetic radiation [14]-[19]. In addition to free-space excitation, RF leaky-wave antennas [20]-[22] have been developed over several decades [23] to produce free-space beams by scattering radiation originating from guided modes. Metasurface concepts have recently advanced this field [19],[24]-[27], but these approaches are not straightforwardly transferable to optical frequencies. For comparison, grating couplers (GCs) in integrated photonics also generate free-space light from in-plane guided sources, but are largely limited in controlling the optical degrees of freedom  $(A, \Phi, \psi, \chi)$  and their spatial profile.

Recent years have seen a rapidly growing interest in incorporating metasurface principles into integrated photonics [28],[29] and, very recently, in generating wavefronts from in-plane guided modes [30]-[38]. This capability is of great interest to the broader optics community, representing a novel opportunity to control off-chip emission of customized free-space wavefronts, while also leveraging on-chip manipulation of light based on the commercially maturing field of photonic integrated circuits (PICs). The customizability of a metasurface-based replacement for GCs offers exciting opportunities for optical communications, augmented reality, quantum optics, and LIDAR. However, so far, the presented approaches offer only partial solutions, not capable of fully controlling the coupling of guided waves to far-field radiation. At most, two optical degrees of freedom have been manipulated at once for a given guided wave, limiting applications to scalar fields (see Supplementary Table S.1 for recent progress in this context).

Additionally, contrary to corrugated structures typically seen in GCs used in integrated photonics [Figs. 1(a,b)], the structures proposed so far are composed of a waveguiding layer and a metasurface as two separate objects [Figs. 1(c,d)], which hinders integrability, scalability, and compactness. In early examples, separated metasurface and GC layers were used [39], while in more recent examples the metasurface was placed in the

evanescent field of the guided mode to both scatter light and manipulate its phase profile. Both metallic [31] and dielectric [34] structures have been explored, introducing either optical loss or high-aspect-ratio dielectric structures typical of metasurface approaches. Adding such lossy or high-aspect-ratio metasurface layer on top of existing waveguiding structures complicates its implementation in comparison to conventional GCs. Additionally, so far these efforts have been limited to small surface emission apertures. These factors hinder the adoption of this approach in PICs. In contrast, a device configuration featuring the compact form factor typical of GCs, and capable of robust, subwavelength control of all four degrees of freedom of light  $(A, \Phi, \psi, \chi)$  introduces a generalization (and where appropriate, replacement) of GCs, advancing existing approaches in both form and function.

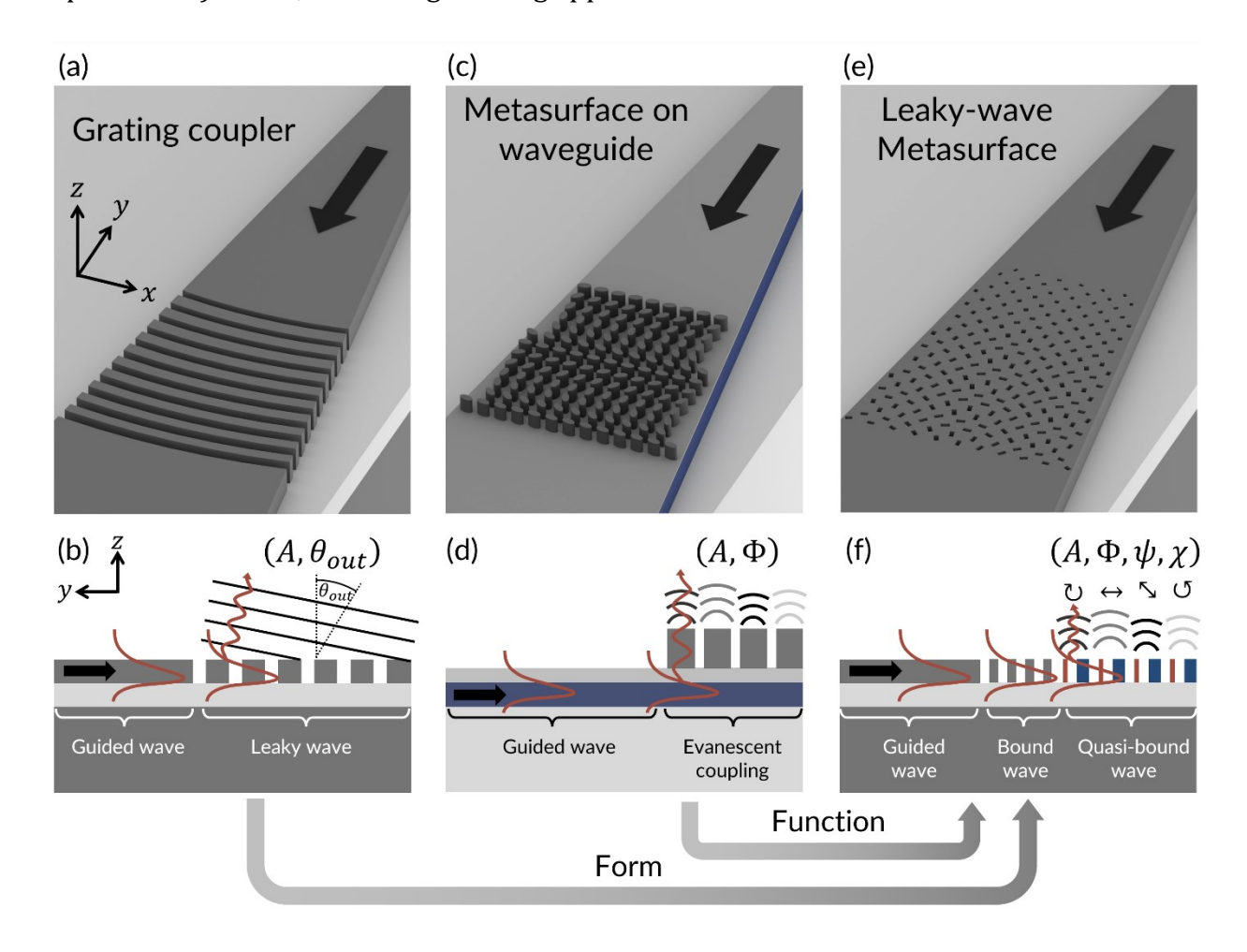


**Figure 1.** Out-coupling in integrated photonic devices. (a) Schematic depiction of a typical GC based on a fully-etched waveguide grating. (b) Side view showing the functionality of a conventional GC, wherein the duty cycle and period may be changed to alter the amplitude and outgoing angle. (c) Schematic depiction of a metasurface-on-waveguide (MOW) device, here based on a high-index dielectric pillar array on a waveguide layer (blue). (d) Side view showing the functionality of a MOW, where the metasurface scatters the evanescent component of a guided wave into the far-field, typically limited to controlling two optical parameters of the surface emission. (e) Schematic depiction of the leaky-wave metasurface (LWM) platform introduced in this work, in which a perturbed (i.e., symmetry-broken) subwavelength photonic crystal slab supports a tailored quasi-bound wave controlling off-chip coupling. (f) Side view showing that the LWM has a compact form equivalent to a GC, but more advanced functionality compared to a MOW, offering simultaneous control over all four degrees of freedom of light  $(A, \Phi, \psi, \chi)$ .

In this work, we introduce a leaky-wave metasurface (LWM) platform, based on weakly corrugated, symmetry-broken photonic crystal slabs, which supports a quasi-bound wave capable of arbitrarily tailoring the scattered field  $(A, \Phi, \psi, \chi)$  with subwavelength resolution [Figs. 1(e,f)]. LWMs inherit the form of GCs, while greatly improving on the functionality of metasurface-on-waveguide solutions. We experimentally implement the proposed concepts in the near-infrared (near  $\lambda$ =1.55 µm) based on a silicon nitride and polymer system, wherein nanostructured polymer zones on an unpatterned silicon nitride thin film define both rib waveguides and LWMs. The design principles are rooted in quasibound states in the continuum [40],[41] and diffractive nonlocal metasurfaces [41]-[45], enabling a rational design approach with largely independent mapping of four geometric parameters to the four optical degrees of freedom. Full-wave simulations are used to create a library of meta-units, each one composed of two staggered rows of ellipse dimers. With simple corrections based on the propagation of the guided mode, reference to this library specifies in a rational way the full geometry of the LWM based on desired spatial profiles of amplitude, phase, and polarization of free-space emission. To demonstrate the flexibility of our platform, we realize focused emission of a desired linear polarization (with wavelength-tuned scanning of the focal spot), a vortex beam generated in concert with a Gaussian reference beam, a two-image hologram encoded in the amplitude and phase of a single polarization, a four-image hologram encoded in the amplitudes and phases of two orthogonal polarizations, and a converging Poincaré beam [46].

Because our platform is designed based on symmetry breaking principles, it exemplifies a universal approach for controlling the leakage of guided waves for a wide range of material systems (e.g., metals, dielectrics, 2D materials) and wave phenomena (e.g., RF, acoustics, elastics, surface waves). Notably, with simple adjustments our approach is compatible with conventional integrated photonic architectures, such as etched waveguides and silicon-on-insulator (SOI) wafers. The methods demonstrated herein can therefore be readily applied to integrated photonic systems, and open a variety of avenues for future research to bridge guided and open systems, ubiquitous across several scientific disciplines.

## Operating principles and metasurface design

The key operating principle of our LWM platform is the deliberate perturbation of a guided mode supported by a periodic structure with subwavelength pitch (i.e., a bound wave under the light line) into a quasi-bound wave (above the light line). As sketched in Fig. 1(f), a guided mode incident from a waveguide couples to a bound wave in the subwavelength periodic structure, and then leaks to free space due to a period-doubling perturbation [47]. For a proof-of-principle, we use the configuration shown in Figs. 2(a,b) based on a rib waveguide and a metasurface defined within a thin layer of polymer ( $n\sim1.48$ ) atop an unpatterned thin film of silicon nitride ( $n\sim2.0$ ) sitting on a silicon dioxide substrate  $(n\sim1.44)$  (see **Methods** for detailed geometrical parameters). The metasurface in its unperturbed state [Fig. 2(c)] is a two-dimensional photonic crystal composed of an oblique lattice of circular holes with pitches  $a_x$  and  $a_y$ ; it supports a bound wave traveling in the -ydirection, whose effective wavelength is approximately  $\lambda_{eff} \approx 2a_y$  . Two independent perturbations are applied to the top pair of circular holes [Fig. 2(d), Perturbation 1] and to the bottom pair of circular holes [Fig. 2(e), Perturbation 2]. These perturbations double the effective lattice pitches to  $2a_x$  and  $2a_y$  and alter the lattice from oblique to rectangular (see **Supplementary Materials S.2**), modifying the first Brillouin zone (FBZ) of the unperturbed lattice [Fig. 2(f)] and its band diagram [Fig. 2(g)] into the zone-folded versions shown in Figs. 2(h,i). The resulting band structure supports transverse-magnetic (TM) modes near  $\lambda_{eff} \approx 2a_v$  in the form of a Dirac point at normal incidence, and red and black arrows in **Figs. 2(g,i)** track example states before and after the perturbation. These arrows span the  $\Gamma$  point of the perturbed band structure, enabling operation anywhere at or near normal to the device plane [48]. We note that an undesirable flat band also arises, degenerate with the

Dirac point when  $a_x = a_y$ , which may be blueshifted or redshifted by detuning from this condition, if desired (see **Supplementary Materials S.3**). In this way, the scheme shown in **Fig. 2** yields a subwavelength lattice that scatters light to free space at or near normal to the device plane, a process exclusively controlled by a geometric perturbation: deliberate engineering of this symmetry-breaking perturbation determines both *if* and *how* the wave leaks to free space, pixel by pixel across the LWM aperture.

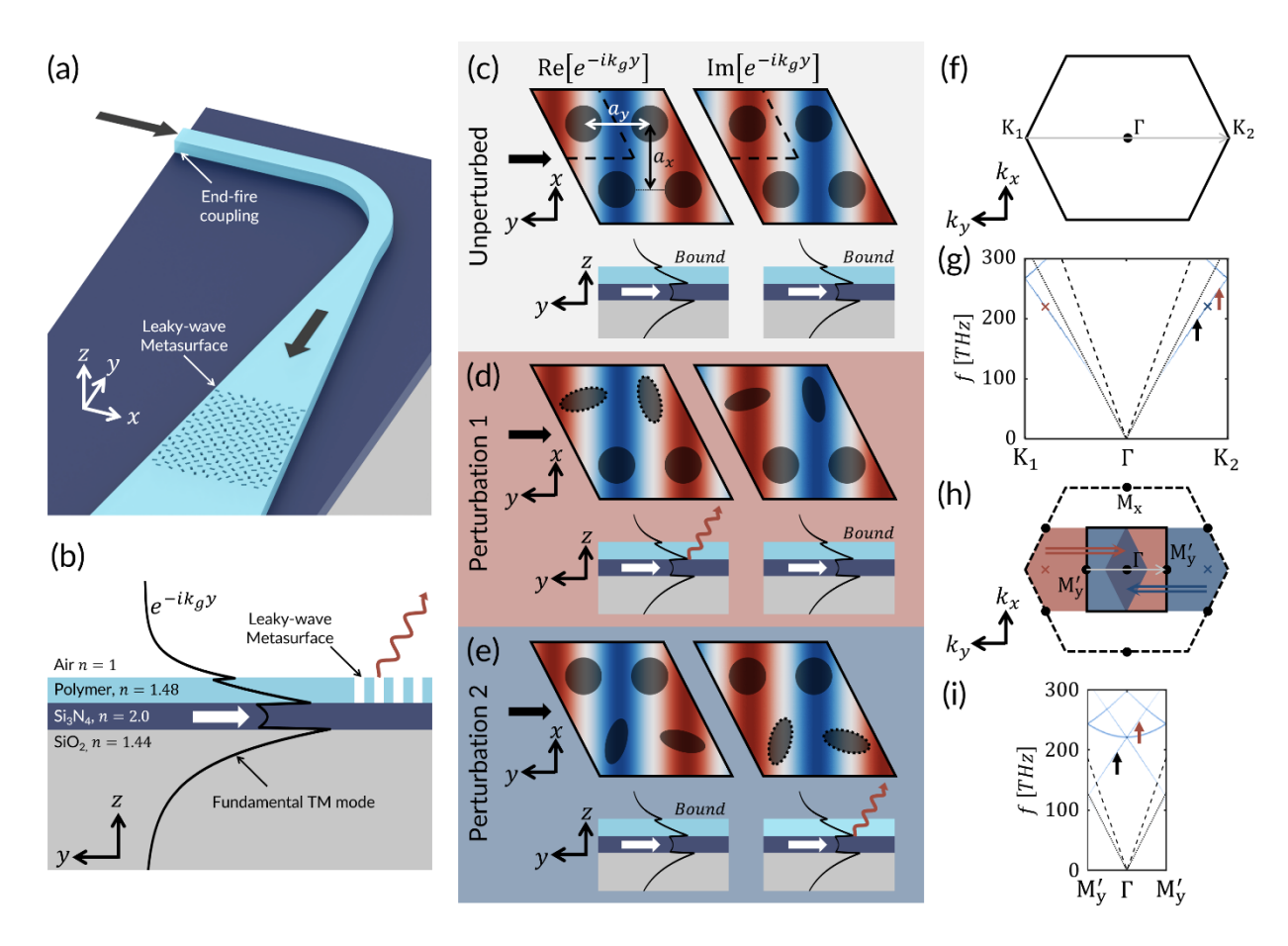


**Figure 2.** Perturbative scheme for rationally designed LWMs. (a) Schematic and (b) side view of the device geometry. (c-e) Perturbative scheme for simultaneous control of the real and imaginary components of the out-of-plane scattered wave. (c) In the unperturbed structure, both the real and imaginary components are bound. (d-e) When the top (bottom) row of circles is perturbed into ellipses (denoted by black dashed boundaries), the real (imaginary) part of the quasi-bound wave is coupled to free space but the imaginary (real) part is not. (f,g) FBZ and TM band diagram of the unperturbed structure. (h,i) FBZ and TM band diagram of the perturbed structure, supporting a zone-folded Dirac point. Modes marked by the arrows in (i) correspond to the those in (g), and red and blue crosses marked

in (h) correspond to those in (g). The dotted and dashed lines in (g,i) denote light cones in the substrate (glass) and superstrate (air), respectively.

The dual-perturbation scheme sketched in **Figs. 2(d,e)** enables independent control of the real and imaginary parts of the scattered light, which together confer complete command over the surface emission:  $(A, \Phi, \psi, \chi)$ . Here we choose the fundamental TM guided mode [depicted in Fig. 2(b)], which, once coupled into the unperturbed subwavelength lattice, is decomposed into its real and imaginary components [Fig. 2(c)]. Each of these components of the travelling TM wave (characterized in the y direction by  $e^{-iky}$ ) is a standing wave of either even or odd parity in the y direction (i.e., cosine or sine). These standing waves abide by selection rules for scattering near the device normal, determining which polarization (if any) couples to free space due to the symmetries broken by the perturbation [41]. The real component is bound except in the presence of Perturbation 1, where the top pair of circles are perturbed into ellipses oriented 90° relative to one another [denoted by the dashed boundaries in Fig. 2(d)]. However, Perturbation 1 does not affect the imaginary component, which is symmetry-protected due to its opposite parity. Perturbation 2 has exactly the opposite effect for the same reason: the imaginary component is scattered while the real component is not [Fig. 2(e)]. These selection rules are intuitively understandable, treating the out-of-plane field components as "charges" and the computing the net "moments" introduced by the perturbations (see Supplementary **Materials S.5** for a discussion).

The behavior of a leaky-wave meta-unit can be modeled analytically in combination with full-wave simulations, as described in **Methods**. **Figure 3(a)** shows two geometric degrees of freedom,  $\delta_1$  and  $\delta_2$ , which determine the sign and strength of each perturbation

and hence the signed magnitude of the real and imaginary components of the scattered light. **Figures 3(b,c)** show the amplitude and phase of the scattered light, which is  $\gamma$ -polarized in this case. At the origin ( $\delta_1 = \delta_2 = 0$ ), a singularity is observed in the phase, corresponding to a null in scattering amplitude, i.e., a bound wave due to the absence of perturbation. This topological feature is a manifestation of the polarization-agnostic geometric phase recently demonstrated to control Fano resonances in nonlocal metasurfaces [49]. Here, we leverage this principle to enable LWMs with complete phase and amplitude (PA) control of any polarization. To produce scattered light with other polarization states, the orientation angles  $\alpha_1$  and  $\alpha_2$  of the ellipses may be varied [Fig. 3(d)]. Figures 3(e,f) show the elliptical parameters,  $\psi$  and  $\chi$  , of the scattered light as a function of  $\alpha_1$  and  $\alpha_2$  , with example polarization states drawn for reference; between the dashed contours, arbitrary elliptical polarization states are possible. Collectively, by varying the geometric parameters  $(\delta_1, \delta_2, \alpha_1, \alpha_2)$ , we can arbitrarily specify the scattered state  $(A, \Phi, \psi, \chi)$ . The mapping between these parameter spaces, including fine adjustments based on full-wave simulations, are discussed in Methods. As a result, we define a semi-analytical library of meta-units for use in populating a LWM that, upon excitation with a guided wave, produces free-space radiation with desired spatial profiles of amplitude, phase, and polarization.

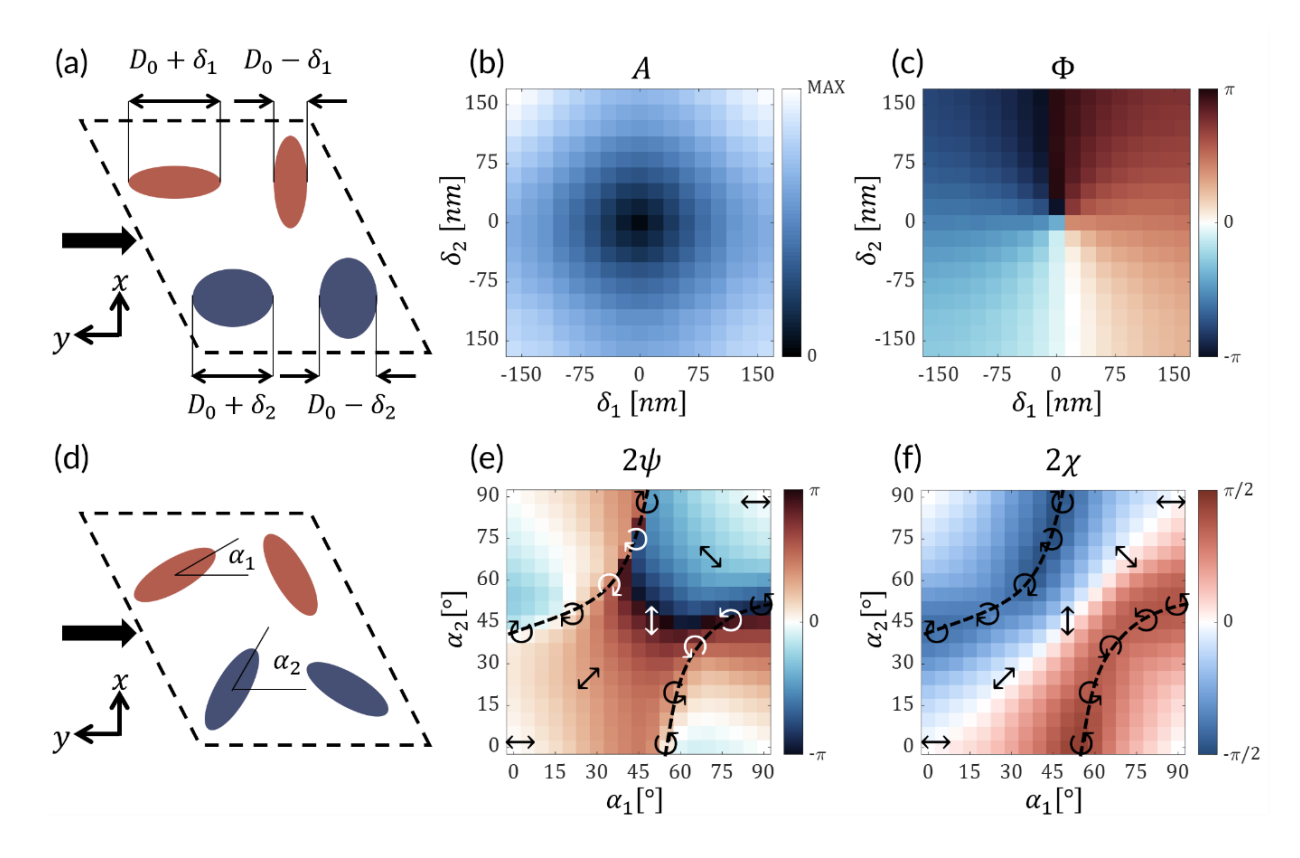


**Figure 3.** Full-wave simulations constructing the meta-unit library. (a) For fixed elliptical orientations, the perturbations  $\delta_1$  and  $\delta_2$  determine the signed magnitude of the real and imaginary parts of the scattered field, respectively. (b) Map of scattered amplitude of y-polarized light as a function of  $\delta_1$  and  $\delta_2$ , showing a bound state when both perturbations vanish. (c) Map of scattered phase of y-polarized light as a function of  $\delta_1$  and  $\delta_2$ , supporting a topological feature characteristic of a geometric phase. (d) For fixed  $\delta_1$  and  $\delta_2$ , the perturbation angles  $\alpha_1$  and  $\alpha_2$  determine the polarization state scattered by the unit cell. (e,f) Map of  $2\psi$  and  $2\chi$  as a function of  $\alpha_1$  and  $\alpha_2$ , with dashed contours denoting chiral states near the poles of the Poincaré sphere. Arrows denoting the approximate polarization states are overlaid for reference.

Finally, the amplitude and phase distributions of the guided portion of the quasibound wave must be accounted for when populating a LWM with meta-units targeting a specific device function (see **Methods** for details). For instance, **Fig. 4(a)** shows a target PA profile producing a focused beam, while **Fig. 4(b)** shows the mode-corrected PA profile, taking into account the amplitude and phase evolution associated with the guided mode depicted in **Fig. 4(c)**. Hence, targeting y-polarized light, **Figs. 4(d,e)** show the resulting profiles of  $\delta_1$  and  $\delta_2$ . The LWM design was then fabricated using electron-beam lithography and characterized in the near-infrared (see **Methods**). An example photo and a scanning electron micrograph of the fabricated devices are shown in **Figs. 4(f,g)**.

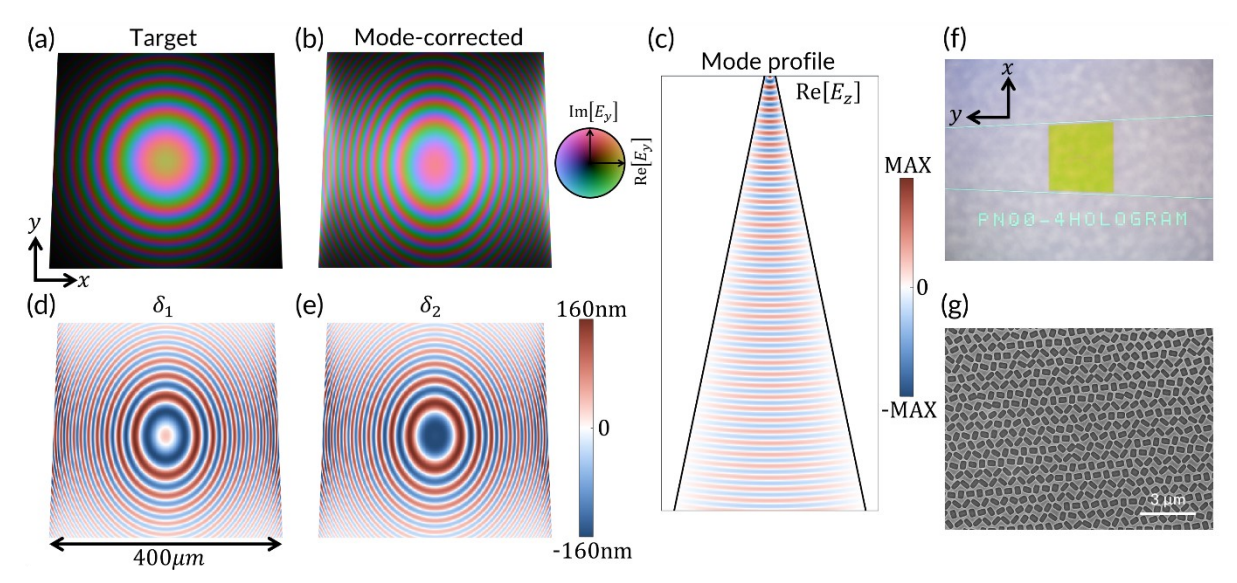


**Figure 4**. Constructing a LWM via modal correction. (a) Target amplitude and phase profiles to produce a converging, linearly polarized beam (y-polarization). (b) Mode-corrected amplitude and phase profiles accounting for the guided mode amplitude and phase profiles in (c). (d,e) Spatial profiles of the perturbation strengths  $\delta_1$  and  $\delta_2$ , populated based on the map in (b) from the meta-unit library. (f) Optical micrograph of a fabricated device. (g) Scanning electron micrograph of a fabricated device.

# Phase and amplitude control

We experimentally demonstrate the ability of our LWM platform to generate custom PA wavefronts. We choose meta-unit motifs with fixed angles  $\alpha_1$  and  $\alpha_2$  so that the wavefronts are linearly polarized. For y-polarized surface emission, we choose  $\alpha_1 = \alpha_2 = 0^\circ$ , while for x-polarized surface emission, we choose  $\alpha_1 = \alpha_2 = 45^\circ$  [Fig. 3(e)]. Figure 5 shows four

example LWMs, demonstrating focusing, generation of orbital angular momentum (OAM), PA holography, and a Kagome lattice generator.

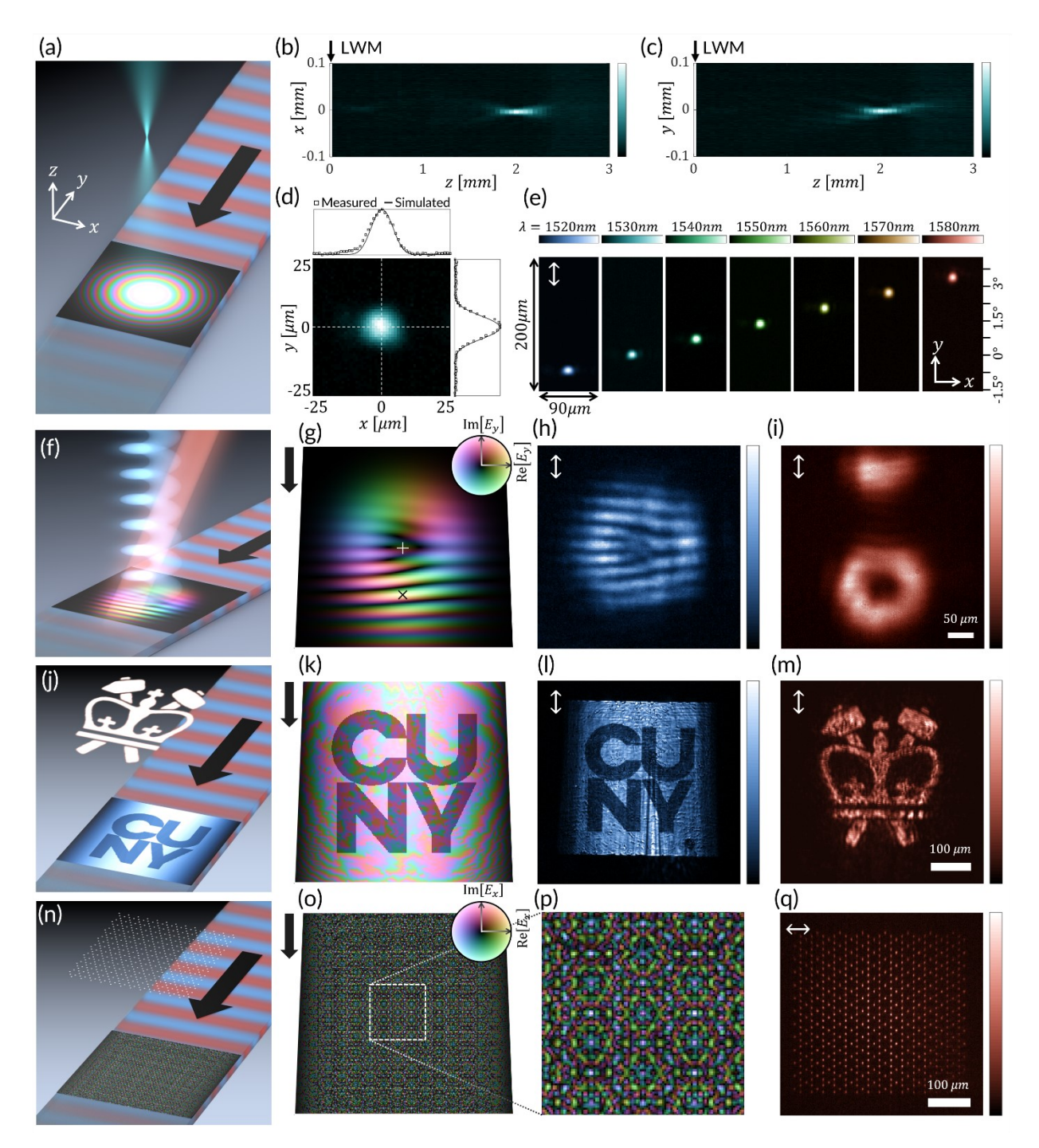


**Figure 5.** Phase-amplitude LWMs for linearly polarized light. (a) Schematic of a focusing LWM. (b,c) Measured xz and yz cross sections showing focused emission from the LWM at  $\lambda_0 = 1550 \ nm$ , with a designed focal length of  $f = 2 \ mm$ . (d) Measured xy cross section at the focal plane for  $\lambda_0 = 1530 \ nm$ , with x and y linecuts compared to simulated responses

based on diffraction limited behavior. (e) Measurement of the focal plane at seven selected wavelengths, demonstrating steering in the *y* direction, following the leaky wave dispersion. (f) Schematic of a LWM producing an OAM beam with  $\ell=2$ , along with a tilted Gaussian beam as a reference, via the complex near field in (g) excited in the direction indicated by the black arrow (the white plus marks the center of the OAM beam emission and the black cross marks the center of the tilted Gaussian beam). (h) Measured interference of the two beams at a plane z = 2 mm, showing a characteristic forked pattern. (i) Measured emission of the OAM device at a plane  $z = 10 \, mm$  away from the LWM, where the OAM and Gaussian beams are separated. (j) Schematic of a two-image hologram, wherein a gray-scale amplitude distribution at the LWM plane serves as a first image, and a distinct holographic image is produced at a second plane based on the phase profile, collectively encoded in the complex near field in (k). (l) Measured gray-scale image (CUNY logo) at the LWM plane. (m) Measured holographic image (Columbia Engineering Logo) at a plane z = 1 mm away from the LWM. (n) Schematic of a Kagome lattice generator based on the complex near field in (o); the central region of this field is shown in (p). (q) Measured holographic lattice at a plane z =0.5 mm away from the LWM. All devices generate y-polarized light, except for the Kagome lattice generator, which produces x-polarized surface emission.

First, **Fig. 5(a)** schematically shows a LWM generating a converging beam in the surface-normal direction. As seen in **Fig. 4(a)**, a Gaussian envelope is applied to the device amplitude profile, and the phase profile of a metalens is encoded to focus light at a target focal length f=2 mm (a numerical aperture of  $NA\approx 0.1$ ). Longitudinal cross-sections of the measured converging beam are shown in **Figs. 5(b,c)**, at  $\lambda=1530$  nm. A transverse cross-section at the designed focal plane is shown in **Fig. 5(d)**, where a focal spot is observed with full-widths at half-maximum (FWHM)  $w_x=10.0\pm0.3~\mu m$  in the x direction and  $w_y=9.1\pm0.1~\mu m$  in the y direction. These values are in good agreement with diffraction-limited operation, with simulated values  $w_x=9.1~\mu m$  and  $w_y=9.4~\mu m$  [insets of **Fig. 5(d)**]. Images of the focal plane at various operating wavelengths from 1520 nm to 1580 nm are shown in **Fig. 5(e)**. The position of the focal spot along the y direction shifts linearly with respect to the wavelength, following the dispersion of the band diagram in **Fig. 2(i)**, with a dispersion

 $\frac{d\theta}{d\lambda} = 1.2 \times 10^{-3} \ rad/nm$ . Measurements confirming the linearly polarized radiation of this device are shown in **Supplementary Materials S.7**.

Next, **Fig. 5(f)** schematically shows a LWM generating a vortex beam with OAM order  $\ell=2$ , in tandem with a tilted wave with a Gaussian profile that serves as an interferometric reference beam [encoded in the complex near field shown in **Fig. 5(g)**]. An image taken at z=2 mm shows the interference of the two beams [**Fig. 5(h)**], where a characteristic fork pattern with two branches is formed (confirming the OAM order), while an image taken at z=10 mm shows the separation of the two beams [**Fig. 5(i)**]. As another example, **Fig. 5(j)** demonstrates a two-image holographic LWM encoded by the two degrees of freedom inherent to a PA metasurface [complex near field shown in **Fig. 5(k)**]. A first image, the CUNY logo is applied as the amplitude profile of the hologram, while a second image, the Columbia Engineering logo, is encoded in the phase profile of the hologram (using the Gerchberg-Saxton algorithm [50]) such that the logo is reconstructed at a distance of z=1 mm (an effective numerical aperture of  $NA \approx 0.2$ ). Images taken at the LWM plane (z=0 mm) and the holographic image plane (z=1 mm) are shown in **Fig. 5(l)** and **Fig. 5(m)**, respectively.

Finally, as a demonstration of the polarization control of our platform, **Fig. 5(n)** depicts a LWM producing a Kagome lattice for x-polarized light via the complex near-field distribution shown in **Fig. 5(o)** [**Fig. 5(p)** shows the central region of this distribution]. Here, the selection rules for the case of  $\alpha_1 = \alpha_2 = 45^\circ$  forbids emission to the y polarization, but allows emission to the x polarization. The measured result at a plane z = 0.5 mm away from the LWM (an effective  $NA \approx 0.37$ ) is shown in **Fig. 5(q)**. Additional devices are reported in **Supplementary Materials S.7** and **S.8**. In particular, three devices are included to demonstrate complete mastery over linear polarization: an x-polarized Fresnel lens and a

device generating radially polarized surface emission in **Supplementary Materials S.7**, and an x-polarized two-image hologram in **Supplementary Materials S.8**. The detailed near-field and geometry profiles of each device in this section and the following section are reported in **Supplementary Materials S.9**. The evolution of optical intensity distributions from the LWM plane to the holographic image plane for the two-image hologram is shown in **Supplementary Materials S.10**.

## **Vector-beam generation**

We next demonstrate LWMs generating vectorial fields. Here, all four geometric degrees of freedom  $(\delta_1, \delta_2, \alpha_1, \alpha_2)$  are utilized to realize PA control for the two orthogonal polarization components simultaneously (i.e., PA profile of a vector beam). **Figures 6(a,b)** schematically show a four-image holographic LWM, extending the scheme in **Figs. 5(j-m)**. Images of the letters " $\psi$ " and " $\chi$ " are applied to the amplitude profiles of the y and x polarization components of the scattered field, while the phase profiles at the two orthogonal polarizations encode the letters "A" and " $\Phi$ ", respectively, for reconstruction at a distance of z=1 mm [**Figs. 6(a,b)**]. Images taken at the holographic image plane (z=1 mm) and the LWM plane (z=0 mm) for the y polarization are shown in **Fig. 6(c)** and **Fig. 6(d)**, respectively; **Figs. 6(e,f)** depict the same for the x polarization.

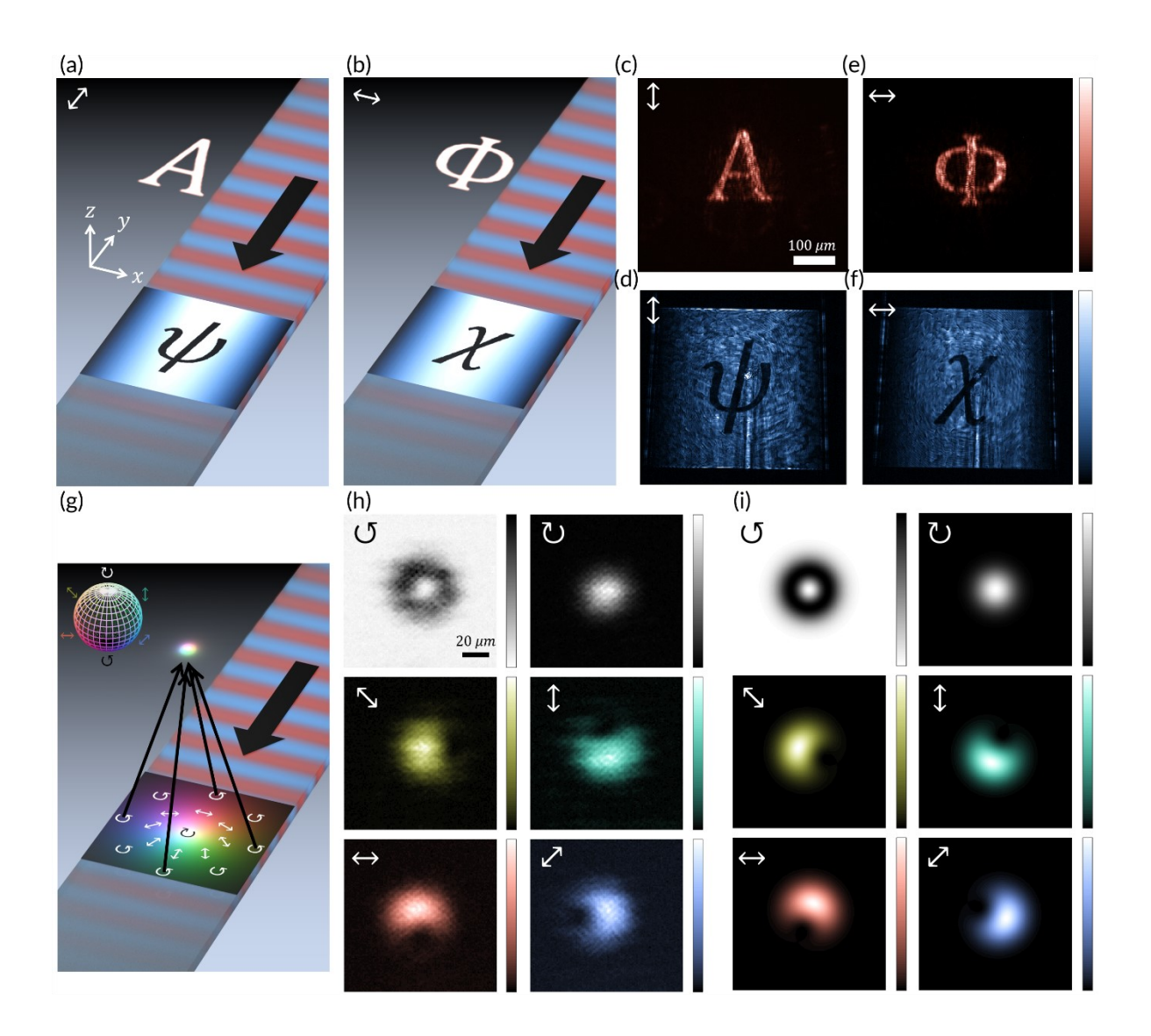


**Figure 6.** Vector-beam LWMs with complete control over amplitude, phase, and polarization. (a,b) Schematic of a LWM producing a four-image hologram, in which two distinct two-image holograms are encoded, respectively, for x and y polarizations. (c,d) Measured y-polarized images at the holographic image ( $z = 1 \, mm$ ) and at the LWM plane ( $z = 0 \, mm$ ), respectively. (e,f) Measured x-polarized images at the holographic image plane ( $z = 1 \, mm$ ) and at the LWM plane ( $z = 0 \, mm$ ), respectively. (g) Schematic of a LWM producing a focusing Poincaré beam. Measured (h) and simulated (i) profiles of six characteristic polarizations at a plane  $z = 2 \, mm$ .

Finally, **Fig. 6(g)** schematically shows a LWM generating a focused Poincaré beam with minimum waist size at a distance of z=2 mm (numerical aperture of  $NA\approx 0.1$ ). Here, we implement the Poincaré beam as the superposition of a focused left-circularly-polarized

(LCP) Gaussian beam and a focused right-circularly-polarized (RCP) vortex beam with  $\ell=1$ , so that a transverse cross-section of the beam reveals all polarization states over the Poincaré sphere [Fig. 6(g)). The four optical degrees of freedom we control in this specific demonstration are the amplitude and phase profiles of the LCP and RCP states. Figure 6(h) shows the measured intensity distributions at a distance z=2 mm and at six characteristic polarization states, in good agreement with the simulated results in Fig. 6(i). The evolution of optical intensity distributions from the LWM plane to the holographic image plane for the four-image hologram is shown in **Supplementary Materials S.10**.

### **Outlook and conclusions**

In this work, we demonstrated complete command over leaky radiation from LWMs through a rational design approach based on quasi-bound states in the continuum that originate from broken symmetries. Our approach confers a number of novelties and advantages compared with other techniques. The novelties center around the period-doubling perturbation, which exclusively introduces coupling to free-space—the mode is otherwise bound. This feature is compatible with large-aperture fields, and here we demonstrated surface emission from integrated devices with a linear dimension  $> 250\lambda_0$ . Large-aperture (millimeter scale and up) fields are highly desirable in a number of applications due to their small divergence angles in the far field (see, e.g., Refs. [51],[52]). The meta-unit motif with two shifted rows of judiciously oriented elliptical apertures enables simultaneous and independent control of amplitude and polarization state of both real and imaginary components of the LWM radiation: the magnitude of the period-doubling perturbation in each row controls the amplitude of each component, while the orientation angle of the perturbation controls the

polarization state. Full control over the polarization state is possible by leveraging symmetry considerations: at perturbation orientation angles  $0^{\circ}$  or  $90^{\circ}$ , x-polarized scattering is forbidden, while at perturbation orientation angles  $\pm 45^{\circ}$ , y-polarized scattering is forbidden; continuity between these extremes guarantees complete polarization control [41,42]. The design's underlying origin in symmetry considerations enables a semi-analytical mapping of the optical degrees of freedom  $(A, \Phi, \psi, \chi)$  to and from the geometric design parameters  $(\delta_1, \delta_2, \alpha_1, \alpha_2)$ . Traditionally, the difficulty of constructing a meta-unit library compounds unfavorably as the number of targeted optical degrees of freedom is increased. Here, in contrast, the LWM geometry is populated point-by-point based on a set of simple equations, while achieving complete control over the vectorial field. Furthermore, the lattice supports a one-dimensional zone-folded Dirac point, enabling operation for frequencies corresponding to at and near the device normal (broadside emission), a feature precluded by the parabolic band structure of modes employed in conventional GC designs.

Our symmetry-based design principle implies that applications involving a wide array of materials and frequencies may adopt this approach. For instance, RF leaky-wave antennas are well-known for beamforming and scanning in the far-field, but are difficult to operate at close range. Our approach may be used to create RF leaky-wave antennas that operate across a wide range of distances, and with distinct functionalities imparted to orthogonal polarizations, useful for polarization-division multiplexing. Similarly, in the context of PICs, while we showed here one popular materials platform based on silicon nitride, the design principle can be applied to silicon-on-insulator technologies. Notably, active materials such as lithium niobate, 2D materials, and liquid crystals may also be incorporated, in order to switch on or off the symmetry-breaking perturbation or to control

its magnitude. Finally, while our LWMs are composed of 2D arrays of holes in a thin film, subwavelength grating waveguides [53] composed of pillars may also be used based on the same principles.

Several extensions may also be explored. First, two-layer devices based on similar period-doubling symmetry-breaking principles have shown exquisite control over the leakage of chiral states [43]. Here, our approach has been primarily achiral: due to the insignificant breaking of out-of-plane symmetry, the upward and downward radiating states are mirror images of each other. In contrast, two-layer devices may add additional control to manipulate separately the upward and downward radiation. Similarly, multi-perturbation devices based on symmetry-breaking have shown control over several leaky waves at distinct frequencies simultaneously [42],[54]. Here, our approach controlled a single mode, but future work may extend the platform to control orthogonally propagating modes (similar to the recent achievements in Ref. [38]). Next, while here we used a weakly corrugated system without deliberate command of the group velocity, band structure engineering (see, e.g., [55], [56]) may be used to tune the angular dispersion of the output. Last, while here we implemented a single device layer, due to the broadband transparency of these nonlocal metasurfaces to free-space light, future works may cascade several LWMs at optically thick distances for multi-wavelength operation [54]. Notably, such cascading scheme is not generically compatible with the MOW approach [Fig. 1(c)].

Finally, we highlight a few improvements that may be explored to further extend the impact of this work. First, while we showed compatibility with large-aperture fields, we made no attempt to optimize the scattering for large radiation efficiency. Future efforts may explore matching the aperture radiation field with the amplitude profile of the quasi-bound

wave to optimally utilize the incident guided wave [57],[58]. As discussed in Supplementary Materials S.11 and S.12, in cases without transverse amplitude modulation of the slab mode (here, in the *x* direction), the radiation efficiency may approach unity by properly designing the profile of the perturbation strength in the propagation direction (here, in the *y* direction). However, in cases with lateral amplitude modulation (e.g., holography), in-plane diffraction may result from local depletion of the slab mode as it propagates. In such cases, the evolution of the slab mode's complex profile must be accounted for by adjusting the sign and strength of the perturbation to match the desired output field. Given maximal achievable scattering strength within the meta-unit library, a minimum device length is required to achieve a target device efficiency. In our case, we estimate this length to be several millimeters, putting our devices in the regime where the majority of optical power remains within the device. In other words, the complications due to depletion of the slab mode are negligible here, at the cost of low device efficiency.

Second, while in our case the flat band observed in Fig. 2(i) did not negatively impact the function of our device, in deeply corrugated structures scattering between the Dirac point and this flat band may introduce unwanted cross-talk. This may be avoided by adjusting the lattice dimensions  $a_x$  and  $a_y$  (Supplementary Materials S.3). Relatedly, while for certain meta-units the Dirac point directly at the  $\Gamma$  point is protected by glide symmetry, in the general case of symmetry-broken meta-units and/or random scattering from fabrication errors, small band gaps or exceptional points [59] may complicate the behavior. For a small range of frequencies (near where the modes cross at the  $\Gamma$  point), the fidelity of the desired responses may suffer in applications requiring extremely collimated light. However, as discussed in Supplementary Materials S.4, due to the perturbative nature of

our approach as well as the low index contrast of our system, these issues are negligible in our present devices; they are minor even in higher index-contrast systems based on SOI.

Last, here we limited our operation to near-normal surface emission (with moderate effective numerical apertures in the range of  $NA \approx 0.1-0.37$ ), allowing us to decouple the real and imaginary components of the scattered wave via their distinct symmetries. At large NA operation or at extreme deflection angles, this assumption may be invalid (to varying degrees in different systems), implying that more complex meta-unit design must be taken into account.

In conclusion, we have introduced a LWM platform that generates custom vectorial fields at will, combining the functionality of metasurfaces with the compact form-factor of GCs. We demonstrated semi-analytical generation of a library of meta-units with complete command over amplitude, phase, and polarization state of light with subwavelength resolution. The design principles are rooted in the symmetries of quasi-bound waves supported by high-symmetry lattices, and are thus compatible with a wide range of materials platforms and frequencies. In the future, we anticipate a number of applications stemming from this approach. Notably, our platform may be integrated with PICs for off-chip communications such as chip-to-chip communications and free-space mode-division multiplexing [e.g., using OAM, Figs. 5(f-i), or Poincaré beams, Figs. 6(g-i)], and it may be used to generate custom cold-atom traps for quantum applications [such as the Kagome lattice in Figs. 5(n-q)]. Our approach may also enable LIDAR systems with optically large apertures for arbitrary beamforming (including broadside emission) and beam steering [Fig. **5(e)**]. Finally, while our implementation employs structural birefringence as a perturbation, small changes in material birefringence (such as in liquid crystals) may achieve similar

control but in a dynamic manner. In this way, our work paves the way towards novel holographic display technologies [Figs. 5(j-m) and Figs. 6(a-f)], quantum photonic devices, and next-generation communications and sensing.

#### Methods

### Modeling and simulations of the meta-units

The Jones vector response of a half meta-unit composed of one pair of ellipses, and excited by a TM slab waveguide mode, approximately follows

$$\binom{E_x}{E_y} = \delta \binom{a_x \sin 2\alpha}{a_y \cos 2\alpha},$$

where  $a_x$  ( $a_y$ ) is the maximum amplitude in the x (y) polarization, which is achieved at maximum  $\delta$  and  $\alpha=45^\circ$  ( $0^\circ$ ). The imbalance between  $a_x$  and  $a_y$  originates from the asymmetry between x and y directions of the system. Here, only the first-order perturbation effect is considered, and in this regime the dependence on  $\delta$  is approximately linear. If the meta-unit is instead excited by a transverse-electric (TE) slab waveguide mode, the Jones vector response will be rotated  $90^\circ$  due to the conversion between E-field and H-field, with an additional constant term in  $E_x$  to account for  $0^{\text{th}}$ -order scattering.

The amplitude A and the polarization orientation angle  $\psi$  of a half meta-unit can be independently controlled by geometric parameters  $\delta$  and  $\alpha$ , respectively. For given target A and  $\psi$ , the corresponding geometric parameters can be explicitly solved:

$$\alpha = \frac{1}{2} \operatorname{arccot} \left( \frac{a_x}{a_y} \tan \psi \right),$$

$$\delta = \frac{A}{a_x} \cos \psi \sqrt{1 + \left(\frac{a_x}{a_y} \tan \psi\right)^2}.$$

For a full meta-unit composed of two pairs of p2 ellipses displaced by a quarter period along the propagation direction, the response is a coherent summation of the two pairs with a  $90^{\circ}$  phase difference:

$$\begin{pmatrix} E_x \\ E_y \end{pmatrix} = \delta_1 \begin{pmatrix} a_x \sin 2\alpha_1 \\ a_y \cos 2\alpha_1 \end{pmatrix} + i\delta_2 \begin{pmatrix} a_x \sin 2\alpha_2 \\ a_y \cos 2\alpha_2 \end{pmatrix},$$

where the first pair of ellipses, characterized by  $(\delta_1, \alpha_1)$ , contributes to the real part, and the second pair of ellipses, characterized by  $(\delta_2, \alpha_2)$ , contributes to the imaginary part. For a complex target  $(E_x, E_y)^T$ , the required geometric parameters can be solved by first calculating the amplitudes  $A_{1,2}$  and polarization orientation angles  $\psi_{1,2}$  of the real and imaginary parts, respectively:

$$A_1 = \sqrt{[\operatorname{Re}(E_x)]^2 + \left[\operatorname{Re}(E_y)\right]^2}, \qquad A_2 = \sqrt{[\operatorname{Im}(E_x)]^2 + \left[\operatorname{Im}(E_y)\right]^2},$$

$$\psi_1 = \arctan \frac{\operatorname{Re}(E_y)}{\operatorname{Re}(E_x)}, \qquad \psi_2 = \arctan \frac{\operatorname{Im}(E_y)}{\operatorname{Im}(E_x)'},$$

then using the above formulas derived for each half meta-unit:

$$\alpha_{1,2} = \frac{1}{2} \operatorname{arccot} \left( \frac{a_x}{a_y} \tan \psi_{1,2} \right),$$

$$\delta_{1,2} = \frac{A_{1,2}}{a_x} \cos \psi_{1,2} \sqrt{1 + \left( \frac{a_x}{a_y} \tan \psi_{1,2} \right)^2}.$$

FDTD simulation results of the polarization ellipticity angle ( $\chi$ ) and the polarization orientation angle ( $\psi$ ) of a leaky-wave meta-unit are shown in **Figs. 3(e,f)**, where  $\alpha_1$  and  $\alpha_2$  are swept from 0° to 90° to cover the polarization space, and  $\delta_{1,2}$  are set according to  $\alpha_{1,2}$  to generate a flat amplitude response. A full coverage of the polarization ellipticity angle from  $\chi = +\pi/4$  (LCP) through  $\chi = 0$  (LP) to  $\chi = -\pi/4$  (RCP) is achieved as  $\alpha_1 - \alpha_2$  varies from

+45° through 0° to -45° [**Fig. 2(f)**], and a full coverage of the polarization orientation angle from  $\psi = -\pi/2$  to  $\psi = \pi/2$  is achieved as  $\alpha_1$  and  $\alpha_2$  vary from 0° to 90° in the  $|\alpha_1 - \alpha_2| < 45$ ° region [**Fig. 3(e)**]. Further simulation results of the amplitude (*A*) and the phase ( $\Phi$ ) responses are shown in **Fig. 3(b)** and **Fig. 3(c)**, respectively, where  $\alpha_1 = \alpha_2 = 0$ ° is set to fix the polarization at  $\chi = \psi = 0$  (y-polarized). Full coverage of amplitude and phase is achieved along the radial [**Fig. 3(b)**] and azimuthal [**Fig. 3(c)**] directions in the parameter sweep, respectively.

Note that this approach assumes that the slab waveguide mode travels along the -y direction, regardless of position across the device. **Supplementary Materials S.6 and S.12** discuss and justify this assumption in more detail, showing that even at the boundaries of the tapered slab waveguide, where the local propagation direction of the guided wave has the largest deviation ( $\sim$ 2.4°) from the -y direction, the change in device performance is negligible. In cases where the above assumption fails, a conformal transformation of the lattice geometry could be explored to align the local lattice parameters with the local guided mode's propagation direction.

The meta-unit responses are simulated via the finite-difference time-domain (FDTD) method (Lumerical). An array of N=9 identical meta-units are placed along the y direction with periodic x boundaries and perfectly matched layers (PMLs) at the y and z boundaries. A total-field scattered-field (TFSF) source is launched in the -z direction, and a mode expansion monitor is placed on the -y side to calculate the complex amplitude of the generated fundamental TM slab waveguide mode. Two separate simulations with x- and y-polarized TFSF sources are performed to obtain the  $E_x$  and  $E_y$  responses, respectively.

#### **Device fabrication**

We experimentally demonstrate LWMs at the telecommunications wavelengths ( $\lambda \approx 1.55 \, \mu m$ ) using a polymer-Si<sub>3</sub>N<sub>4</sub> materials platform. Both the waveguide circuit and the meta-unit holes composing the metasurface are patterned in a 300-nm poly(methyl methacrylate) or PMMA layer, on the top of a 300-nm Si<sub>3</sub>N<sub>4</sub> thin film, on a SiO<sub>2</sub> substrate. The fundamental TM guided mode is fed from a single-mode ridge waveguide via a linear taper with a tapering rate of  $\Delta w/\Delta L = 1/12$ . A LWM device with a linear dimension of ~400  $\mu$ m is integrated within the taper (**Fig. 4f**). The amplitude and phase distributions in the tapered slab waveguide are nonuniform, which should be compensated for when designing the LWM amplitude and phase profiles. Expanded from a single-mode waveguide through a linear taper, the slab waveguide mode can be approximated with an analytic expression:

$$E(x,y) = E_0 A(x,y) e^{i\phi(x,y)},$$

with

$$A(x,y) = \sqrt{\frac{w_0}{w(y)}} \cos\left[\frac{\pi x}{w(y)}\right] e^{\frac{\alpha y}{2}},$$

$$\phi(x,y) = \frac{2\pi}{\lambda} \left[ -n_{ms}y + n_{wg} \frac{x^2}{2(L-y)} \right],$$

where the amplitude distribution A(x,y) is formed by the collective effects of: (i) waveguide widening, i.e.,  $w(y) = w_0 + \Delta w/\Delta L \cdot (L-y)$ , where  $L \approx 4800$  µm is the taper length and y is the longitudinal coordinate, (ii) transverse waveguide mode profile associated with the local waveguide width w(y), and (iii) attenuation due to out-coupling from the metasurface; the phase distribution  $\phi(x,y)$  is composed of: (i) longitudinal phase accumulation in the metasurface region with an effective modal index  $n_{ms} \approx 1.52$ , and (ii) transversal phase

profile in the linear taper with an effective modal index  $n_{wg} \approx 1.55$ , approximated by a paraxial cylindrical wave.

Finally, the devices are fabricated as follows.  $Si_3N_4$  thin films of 300 nm thickness are grown via plasma-enhanced chemical vapor deposition on a fused silica substrate of 180  $\mu$ m thickness. A 300-nm PMMA layer is spin coated and baked at 180 °C to serve as an electron-beam resist. Electron-beam lithography (Elionix ELS-G100) is then carried out at 100 keV and 1 nA, with a dose of 750  $\mu$ C/cm² and appropriate proximity effect corrections (BEAMER), to define the waveguide boundaries and LWM patterns. A 3:1 mixture of isopropyl alcohol to deionized water is used to develop the exposed resist. The fabricated chip is then cleaved to expose the facet of the narrow single-mode ridge waveguide for fiber coupling.

#### **Device characterization**

Near-infrared light at  $\lambda \approx 1.55~\mu m$  is generated by a diode laser, and coupled into the LWM device using a lensed optical fiber with proper polarization adjustment. The surface emission on the air side produced by the device is collected by a  $10\times$  or  $20\times$  near-infrared objective (Mitutoyo), passed through a polarization filter (Thorlabs), and directed towards a near-infrared camera (Princeton Instruments).

#### **Acknowledgements**

This work was supported by the National Science Foundation (grant no. QII-TAQS-1936359 and no. ECCS-2004685), the Air Force Office of Scientific Research (no. FA9550-16-1-0322), and the Simons Foundation. S.C.M. acknowledges support from the NSF Graduate Research Fellowship Program (grant no. DGE-1644869). Device fabrication was carried out at the Columbia Nano Initiative cleanroom, and at the Advanced Science Research Center NanoFabrication Facility at the Graduate Center of the City University of New York.

#### **Author contributions**

A.C.O and H.H. conceived the idea. H.H. and A.C.O mathematically modeled the devices and performed simulations. H.H. designed and fabricated the devices. H.H., A.C.O., Y.X., S.C.M., C.-C. T., and N.Y. characterized the devices. A.C.O and H.H. analyzed the data. A.C.O., H.H., A.A., and N.Y. wrote the manuscript. A.A. and N.Y. supervised the research.

## **Competing interests**

The authors declare no competing interests.

## **References**

- [1] N. Yu et al., "Light Propagation with Phase Discontinuities: Generalized Laws of Reflection and Refraction", Science 334, 333 (2011).
- [2] N. Yu and F. Capasso, "Flat optics with designer metasurfaces", *Nat. Mater.* **13** 139-150 (2014).
- [3] P. Lalanne, S. Astilean, P. Chavel, E. Cambril, H. Launois, "Blazed binary subwavelength gratings with efficiencies larger than those of conventional echelette gratings", *Optics Letters* **23**, 108101083 (1998).
- [4] S. Chen. W. Liu, Z. Li, H. Cheng, and J. Tian, "Metasurface-Empowered Optical Multiplexing and Multifunction", *Adv. Mater.* **32**, 185912 (2020).
- [5] M. Kim, A.M.H. Wong, G.V. Eleftheriades, "Optical Huygens' Metasurfaces with Independent Control of the Magnitude and Phase of the Local Reflection Coefficients", Phys. Rev. X 4, 041042 (2014).

- [6] A.C. Overvig, S. Shrestha, S.C. Malek, M. Lu, A. Stein, C. Zheng, and N. Yu, "Dielectric metasurfaces for complete and independent control of the optical amplitude and phase", Light Sci. Appl. **8**, 92 (2019).
- [7] A. Arbabi, Y. Horie, M. Bagheri, and A. Faraon, "Dielectric Metasurfaces for Complete Control of Phase and Polarization with Subwavelength Spatial Resolution and High Transmission", Nat. Nanotech. **10**, 937-943 (2015).
- [8] J.P. Balthasar Mueller, N. A. Rubin, R. C. Devlin, B. Groever, and F. Capasso, *Phys. Rev. Lett.* **118**, 113901 (2017).
- [9] Y. Bao, J. Ni, and C-W. Qiu, "A Minimalist Single-Layer Metasurface for Arbitrary and Full Control of Vector Vortex Beams", Adv. Mat. **32**, 1905659 (2020).
- [10] Z. L. Deng, M. Jin, X. Ye, S. Wang, T. Shi, J. Deng, N. Mao, Y. Cao, B.O. Guan, A. Alu, G. Li, and X. Li, "Full-Color Complex-Amplitude Vectorial Holograms Based on Multi-Freedom Metasurfaces", Adv. Func. Mat., 30, 1910610 (2020).
- [11] M. Liu, W. Zhu, P. Huo, L. Feng, M. Song, C. Zhang, L. Chen, H. J. Lezec, Y. Lu, A. Agrawal, and T. Xu, "Multifunctional metasurfaces enabled by simultaneous and independent control of phase and amplitude for orthogonal polarization states", *Light: Sci. & Appl.* **10**, 107 (2021).
- [12] T. Wu, X. Zhang, Q. Xu, E. Plum, K. Chen, Y. Xu, Y. Lu, H. Zhang, Z. Zhang, X. Chen, G. Ren, L. Niu, Z. Tian, J. Han, and W. Zhang, "Dielectric Metasurfaces for Complete Control of Phase, Amplitude, and Polarization", Adv. Opt. Mater. 10, 2101223 (2022).
- [13] Y. Bao, L. Wen, Q. Chen, C.-W. Qiu, and B. Li, "Toward the capacity limit of 2D planar Jones matrix with a single-layer metasurface", *Sci. Adv.* **7**, eabh0365 (2021).

- [14] Y. Svirko, N. Zheludev, and M. Osipov, "Layered chiral metallic microstructures with inductive coupling", *Appl. Phys. Lett.* **96**, 203501 (2010).
- [15] N. Kanda, K. Konishi, and M. Kuwata-Gonokami, "Terahertz wave polarization rotation with double layered metal grating of complimentary chiral patterns", *Opt. Express* **15**, 11117-111125 (2007).
- [16] A. Epstein, and G.V. Eleftheriades, "Arbitrary antenna arrays without feed networks based on cavity-excited omega-bianisotropic metasurfaces", *IEEE Trans. Antennas Propag.* **65**, 1749-1756 (2017).
- [17] Y. Ra'di, V.S. Asadchy, and S.A. Tretyakov, "Tailoring reflections from thin composite metamirrors", *IEEE Trans. Antennas Propag.* **62**, 3749-3760 (2015).
- [18] Y. Yuan, K. Zhang, B. Ratni, Q. Song, X. Ding, Q. Wu, S. N. Borokur, and P. Genevet, "Independent phase modulation for quadruplex polarization channels enabled by chirality-assisted geometric-phase metasurfaces", *Nature Comm.* **11**, 4186 (2020).
- [19] A. Li, S. Singh, and D. Sievenpiper, "Metasurfaces and their applications", *Nanophotonics* **7**, 989-1011 (2018).
- [20] T. Tamir and A. A. Oliner, "Guided Complex Waves-Part I: Fields at an Interface", *Proc. Inst. Elec. Eng.* (London), **110**, 310-324 (1963).
- [21] T. Tamir and A. A. Oliner, "Guided Complex Waves-Part II: Relation to Radiation Patterns", *Proc. Inst. Elec. Eng.* (London), **110**, 325-334 (1963).
- [22] D.R. Jackson, and A. A. Oliner, "A Leaky-Wave Analysis of the High-Gain Printed Antenna Configuration", *IEEE Trans. Antennas Popag.* **36**, 905-910 (1988).

- [23] D. R. Jackson and A. A. Oliner, "Leaky-Wave Antennas". Modern Antenna Handbook, edited by Constantine A. Balanis, Wiley, pp. 325-367 (2008). DOI: 10.1002/9780470294154.ch7
- [24] F. Monticone and A. Alu, "Leaky-Wave Theory, Techniques, and Applications: From Microwaves to Visible Frequencies", *Proc. of the IEEE*, **103** 793-821 (2015).
- [25] G. Minatti, F. Caminita, M. Casaletti, and S. Maci, "Spiral leaky-wave antennas based on modulated surface impedance", *IEEE Trans. Antennas Propag.* **59**, 4436-4444 (2011).
- [26] B. B. Tienrey, and A. Grbic, "Controlling Leaky Waves with 1-D Casacaded Metasurfaces", *IEEE Trans. Antennas Popag.* **66**, 2143-2146 (2018).
- [27] E. Abdo-Sanchez, M. Chen, A. Epstein, and G. V. Eleftheriades, "A Leaky-Wave Antenna With Controlled Radiation Using a Bianistropic Huygens' Metasurface", *IEEE Trans. Antennas Propag.* **67** 108-120 (2019).
- [28] Y. Meng, et al. "Optical meta-waveguides for integrated photonics and beyond", Light: Sci. & Appl. 10, 235 (2021).
- [29] Z. Li, M.-H. Kim, C. Wang, Z. Han, S. Shrestha, A. C. Overvig, M. Lu, A. Stein, A. M. Agarwal, M. Loncar, and N. Yu, "Controlling propagation and coupling of waveguide modes using phase-gradient metasurfaces", *Nat. Nanotech.* **12**, 675-683 (2017).
- [30] Z. Huang, D. L. Marks, and D. R. Smith, "Out-of-plane computer-generated multicolor waveguide holography", *Optica* **6**, 119-124 (2019).
- [31] X. Guo, Y. Ding, X. Chen, Y. Duan, and X. Ni, "Molding free-space light with guided wave-driven metasurfaces", *Sci. Adv.* **17**, eabb4172 (2020).
- [32] L. Li, K. Yao, Z. Wang, and Y. Liu, "Harnessing Evanescent Waves by Bianisotropic Metasirfaces", *Laser & Photonics Rev.* **14**, 1900244 (2020).

- [33] Y. Ha, Y. Guo, M. Pu, X. Li, X. Ma, Z. Zhang, and X. Luo, "Monolithic-Integrated Multiplexed Devices Based on Metasurface-Driven Guided Waves", *Adv. Theory and Sim.* **4**, 2000239 (2021).
- [34] B. Fang, Z. Wang, S. Gao, S. Zhu, and T. Li, "Manipulating guided wave radiation with integrated geometric metasurface" *Nanophotonics* **11**, 1923-1930 (2022).
- [35] Y. Deng, X. Chen, T. Duan, H. Huang, L. Zhang, S. Chang, X. Guo, and X. Ni, "Metasurface-Dressed Two-Dimensional on-Chip Waveguide for Free-Space Light Field Manipulation".

  ACS Photonics 9, 398–404 (2022).
- [36] C. Xie, L. Huang, W. Liu, W. Hong, J. Ding, W. Wu, and M. Guo, "Bifocal focusing and polarization demultiplexing by a guided wave-driven metasurface", *Opt. Exp.* **29**, 25709-25719 (2021).
- [37] R. Yang, S. Wan, Y. Shi, Z. Wang, J. Tang, and Z. Li, "Immersive Tuning the Guided Waves for Multifunctional On-Chip Metaoptics", *Laser & Photonics Rev.* **16**, 2200127 (2022).
- [38] Y. Shi, C. Wan, C. Dai, S. Wan, Y. Liu, C. Zhang, and Z. Li, "On-chip meta-optics for semi-transparent screen display in sync with AR projection", *Optica* **9**, 670-676 (2022).
- [39] A. Yulaev, W. Zhu, C. Zhang, D. A. Westly, H. J. Lezec, A. Agrawal, and V. Aksyuk, "Metasurface-Integrated Photonic Platform for Versatile Free-Space Beam Projection with Polarization Control", *ACS Photonics* **6**, 2902-2909 (2019).
- [40] K. Koshelev, S. Lepeshov, M. Liue, A. Bogdanov, and Y. Kivshar, Asymmetric metasurfaces with high-Q resonances governed by bound states in the continuum, *Phys. Rev. Lett.* **121**, 193903 (2018).
- [41] A.C. Overvig, S. C. Malek, M. J. Carter, S. Shrestha, and N. Yu, "Selection rules for quasibound states in the continuum", *Phys. Rev. B* **102**, 035434 (2020).

- [42] A.C. Overvig, S. C. Malek, and N. Yu, "Multifunctional Nonlocal Metasurfaces", Phys. Rev. Lett. **125**, 017402 (2020).
- [43] A.C. Overvig, N. Yu, and A. Alù, "Chiral Quasi-Bound States in the Continuum", *Phys. Rev. Lett.* **126**, 073001 (2020).
- [44] A.C. Overvig and A. Alu, "Diffractive Nonlocal Metasurfaces", *Laser & Photon. Rev.* **16**, 2100633 (2022).
- [45] M. Lawrence, D. R. Barton III, J. Dixon, E. Klopfer, S. Dagli,, M. L. Brongersma, and J. A. Dionne, "High quality factor phase gradient metasurfaces", *Nat. Nanotechnol.* **15**, 956-961 (2020).
- [46] A. M. Beckley, T. G. Brown, and M. A. Alonso, "Full Poincaré beams", *Optics Express* **18**, 10777-10785 (2010).
- [47] A.C. Overvig, S. Shrestha, and N. Yu, "Dimerized high contrast gratings", *Nanophotonics* **7**, 1157 (2018).
- [48] M. Memarian, and G. V. Eleftheriades, "Dirac leaky-wave antennas for continuous beam scanning from photonic crystals", *Nat. Comm.* **6**, 5855 (2015).
- [49] A. Overvig, Y. Kasahara, X. Gu, and A. Alu, "Complete Command of Scattering in Diffractive Nonlocal Metasurfaces Supporting a Polarization-Agnostic Geometric Phase", [Submitted].
- [50] R. W. Gerchberg, and W. O. Saxton, "A practical algorithm for the determination of the phase from image and diffraction plane pictures", *Optik* **35**, 237-246 (1972).
- [51] C.V. Poulton, M.J. Byrd, M. Raval, Z. Su, N. Li, E. Timurdogan, D. Coolbaugh, D. Vermeulen, and M.R. Watts, "Large-scale silicon nitride nanophotonic phase arrays at infrared and visible wavelengths", *Opt. Lett.* **42**, 21-24 (2017).

- [52] N. Chauhan, D. Bose, M. Puckett, R. Moreira, K. Nelson, D. Bluemnthal, "Photonic Integrated Si3N4 Ultra-Large-Area Grating Waveguide MOT Interface for 3D Atomic Clock Laser Cooling", in *Conference for Lasers and Electro-Optics (CLEO)* (2019).
- [53] P. Cheben, R. Halir, J. H. Schmid, H. A. Atwater, and D. R. Smith, "Subwavelength integrated photonics", *Nature* **560**, 565-572 (2018).
- [54] S. C. Malek, A. C. Overvig, A. Alu, and N. Yu, "Multifunctional Resonant Wavefront-Shaping Meta-Optics Based on Multilayer and Multi-Perturbation Nonlocal Metasurfaces", *Light: Sci. & Appl.* **11**, 246 (2022).
- [55] R. Magnusson, M. Shokooh-Saremi, and X. Wang, "Dispersion Engineering with Leaky-Mode Resonant Photonic Lattices", *Opt. Exp.* **18**, 108-116 (2010).
- [56] H. S. Nguyen, F. Dubois, T. Deschamps, S. Cueff, A. Pardon, J.-L. Leclercq, C. Seassal, X. Letartre, and P. Viktorovitch, "Symmetry Breaking in Photonic Crystals: On-Demand Dispersion from Flatband to Dirac Cones", *Phys. Rev. Lett.* **120**, 066102 (2018).
- [57] K.A. Bates, L. Li, R.L. Roncone, and J.J. Burke, "Gaussian beams from variable groove depth grating couplers in planar waveguides", *Applied Optics* **32**, 2112-2116 (1993).
- [58] Z. Zhao and S. Fan, "Design Principles of Apodized Grating Couplers", J. Light. Technol. 38, 4435-4446 (2020).
- [59] A. Yulaev, S. Kim, Q. Li, D.A. Westly, B.J. Roxworthy, K. Srinivasan, and V.A. Aksyuk, "Exceptional points in lossy media lead to deep polynomial wave penetration with spatially uniform power loss", *Nat. Nanotechnol.* **17**, 583-589 (2022).